

Ab initio description of heterostructural alloys: Thermodynamic and structural properties of $\text{Mg}_x\text{Zn}_{1-x}\text{O}$ and $\text{Cd}_x\text{Zn}_{1-x}\text{O}$

A. Schleife, M. Eisenacher, C. Rödl, F. Fuchs, J. Furthmüller, and F. Bechstedt

Institut für Festkörperteorie und -optik, Friedrich-Schiller-Universität and European Theoretical Spectroscopy Facility (ETSF), Max-Wien-Platz 1, 07743 Jena, Germany

(Received 19 March 2010; revised manuscript received 4 May 2010; published 17 June 2010)

Pseudobinary heterostructural alloys of ZnO with MgO or CdO are studied by composing the system locally of clusters with varying ratio of cations. We investigate fourfold (wurtzite structure) and sixfold (rocksalt structure) coordination of the atoms. By means of density-functional theory, we study a total number of 256 16-atom clusters divided into 22 classes for the wurtzite structure and 16 classes for the rocksalt structure for each of the alloy systems. The fraction with which each cluster contributes to the alloy is determined for a given temperature T and composition x within (i) the generalized quasichemical approximation, (ii) the model of a strict-regular solution, and (iii) the model of microscopic decomposition. From the cluster fractions, we derive conclusions about the miscibility and the critical compositions at which the average crystal structure changes. Thermodynamic properties such as the mixing free energy and the mixing entropy are investigated for the three different statistics. We discuss the consequences of the two different local lattice structures for characteristic atomic distances, cohesive energies, and the alloys' elasticities. The differences in the properties of $\text{Mg}_x\text{Zn}_{1-x}\text{O}$ and $\text{Cd}_x\text{Zn}_{1-x}\text{O}$ are explained and discussed.

DOI: [10.1103/PhysRevB.81.245210](https://doi.org/10.1103/PhysRevB.81.245210)

PACS number(s): 61.66.Dk, 64.75.-g, 62.20.-x

I. INTRODUCTION

Recently, ZnO has attracted renewed attention as a closely lattice-matched substrate for GaN and also as a potentially useful active optoelectronic material in its own right.¹⁻⁴ When doped with Al, it plays a role as a transparent conducting oxide in solar cells⁵ but also microelectronic and sensory devices may be fabricated involving oxides such as ZnO.^{6,7} Further, it is environmentally friendly, biocompatible, and tends to form nanostructures.⁸

The tailoring of material properties is an important reason for combining ZnO with other group-II oxides in alloys and heterostructures. Mixed $\text{Mg}_x\text{Zn}_{1-x}\text{O}$ crystals allow to tune the energy gap from about 3.4 eV of wurtzite (wz) ZnO toward the ultraviolet spectral region with at least 4.4 eV in $\text{Mg}_x\text{Zn}_{1-x}\text{O}$.⁹⁻¹¹ Conversely, pseudobinary $\text{Cd}_x\text{Zn}_{1-x}\text{O}$ alloys tend to close the gap and are, therefore, suitable candidates for optoelectronic devices in the visible spectral range.¹² Moreover, quantum-well and other heterostructures based on the combinations $\text{Mg}_x\text{Zn}_{1-x}\text{O}/\text{ZnO}$ and $\text{ZnO}/\text{Cd}_x\text{Zn}_{1-x}\text{O}$ allow an additional tailoring of electronic and optical properties by means of quantum-confinement effects.^{6,12,13}

The combination of these group-II oxides in alloys and heterostructures raises several fundamental questions since there is a crystal structure mismatch: while some binary II-VI compounds occur in the fourfold-coordinated wz structure (e.g., ZnO), others show the sixfold-coordinated rocksalt (rs) structure (e.g., MgO and CdO) under ambient conditions.^{14,15} Isovalent and isostructural alloys of II-VI constituents are generally thermodynamically unstable because their mixing enthalpy in either the rs structure or the wz structure is positive.¹⁶ A thermodynamical miscibility only exists at very high temperatures, i.e., where the mixing entropy is sufficiently large; at lower temperatures there is a tendency for a phase separation of the alloys.¹⁷ However, isovalent but heterostructural II-VI alloys seem to be stable

under certain conditions: $X_x\text{Zn}_{1-x}\text{O}$ alloy films occur in wz structure for $x < 0.55$ ($X = \text{Mg}$) (Refs. 18–20) or $x < 0.32$ ($X = \text{Cd}$, grown under nonequilibrium conditions).^{12,13} Depending on the composition x , the film preparation may give rise to a nonuniformity of pseudobinary thin films as observed experimentally for $\text{Mg}_x\text{Zn}_{1-x}\text{O}$.²¹ With increasing molar fractions x (Mg or Cd content), a change in the coordination (fourfold to sixfold) of the atoms is expected. Both hexagonal and cubic $\text{Mg}_x\text{Zn}_{1-x}\text{O}$ thin films are reported.²² The situation in pseudobinary $\text{Cd}_x\text{Zn}_{1-x}\text{O}$ is less clear. The rs structure of CdO seems to limit the equilibrium solubility in wz-ZnO to molar fractions below $x = 0.07$.^{23,24} On the other hand, metal-organic chemical vapor deposition (MOCVD) techniques produced alloys up to $x = 0.7$.¹³ Molecular beam epitaxy (MBE) leads to epilayers with a structure close to the wz one without an indication for a phase separation up to a Cd concentration of $x = 0.32$.¹²

Summarizing, there is no microscopic picture of how the heterostructural aspect influences the properties of isovalent pseudobinary alloys with oxygen as anion. Stability, solubility, and tendency of decomposition of systems such as $\text{Mg}_x\text{Zn}_{1-x}\text{O}$ or $\text{Cd}_x\text{Zn}_{1-x}\text{O}$ are barely understood so is their different behavior. One reason is that most of the existing theoretical studies are limited to ordered structures such as MgZnO_2 (Refs. 25 and 26) or somewhat more complex geometries.¹⁶

On the other hand, the theoretical methods for the description of the thermodynamic and structural properties of pseudobinary alloys of the type $\text{A}_x\text{B}_{1-x}\text{C}$ have been developed over the last 20 years. A basic approach is to simulate the configurational average by representing all possible occurring local bonding configurations using certain crystal geometries. There is one study²⁷ in which the chemically disordered $\text{Mg}_x\text{Zn}_{1-x}\text{O}$ alloys have been simulated using special quasirandom structures.²⁸ In another approach,^{29,30} the mixing free energy of a random alloy is described combining a

cluster-expansion method^{31–33} with the generalized quasicheical approximation (GQCA).³⁴ In several publications about pseudobinary alloys with the first-row elements N or O as anions,^{27,30,35} this method has been applied together with an *ab initio* description of total energies and atomic geometries. However, in all these studies, the (local) crystal structure has been fixed being wz, zinblend, or rs. Only recently, the isovalent but heterostructural MgO-ZnO system has been studied by combining the rs with the wz crystal structure within a cluster expansion.^{16,36} Energetic stability has been found in the sixfold-coordinated structure for Zn concentrations below 67%, giving rise to spontaneously ordered alloys.¹⁶ Without a configurational average, i.e., by studying only certain clusters with fixed molar fractions,³⁶ no conclusions are possible for different growth situations. Coherent-potential approximation calculations³⁷ for various crystal phases allowed for the construction of a phase diagram with a phase transition from wz to rs close to $x=0.33$. However, the coherent-potential approximation, as a single-site theory, is expected to be more reliable close to the binary end components whereas for intermediate compositions x , the single-site approximation is questionable.

In this paper, we extend the generalized quasicheical approach for one local crystal structure to alloys that consist of two binary compounds with two different equilibrium crystal structures, i.e., rs and wz. The results of the GQCA are compared to two other cluster statistics, which may be considered as limiting cases of the GQCA with respect to the number of possible atom arrangements. The theory is applied to heterostructural $\text{Mg}_x\text{Zn}_{1-x}\text{O}$ and $\text{Cd}_x\text{Zn}_{1-x}\text{O}$ alloys. In Sec. II, we present a cluster expansion for the rs crystal structure along with the combined statistics that deals with wz and rs clusters simultaneously. The computational approaches that are used for carrying out the actual calculations are explained in Sec. III. Results for the thermodynamic properties are given in Sec. IV and for the structural and elastic properties in Sec. V. Finally, Sec. VI concludes the paper.

II. ALLOY STATISTICS AND THERMODYNAMICS

A. Cluster expansion for wurtzite and rocksalt structures

We study pseudobinary alloys $\text{A}_x\text{B}_{1-x}\text{C}$ with N atoms of type C on the anion sublattice and N atoms of type A or B on the cation sublattice. Within a cluster-expansion method,^{29–32,34} the macroscopic alloy is divided into an ensemble of M clusters consisting of $2n$ atoms (n anions and n cations) each. The total number of cations or anions is then given by $N=nM$.

From combinatorics, it follows that, for a given crystal structure, there are 2^n different possibilities of arranging A- or B-type atoms on the n cation sites of one cluster (the occupation of the anion sublattice is fixed). Due to the symmetry of the crystal lattice, the clusters can be grouped in $J+1$ different classes, with J depending on the actual crystal structure. Each class $j(j=0, \dots, J)$ contains g_j clusters of the same total energy ε_j , with the degeneracy factors g_j fulfilling the relation $\sum_j g_j = 2^n$.

To each macroscopic alloy, one can assign a cluster set $\{M_0, M_1, \dots, M_J\}$ which describes how many clusters of each

class occur in the alloy. A single class j contributes to the macroscopic alloy with its cluster fraction x_j that is defined by $x_j=M_j/M$. The x_j fulfill the constraint,

$$\sum_{j=0}^J x_j = 1, \quad (1)$$

which stems directly from the relation $M=\sum_j M_j$ for the cluster set. The n cation sites of each cluster are occupied with n_j atoms of species A and $(n-n_j)$ atoms of species B. Since the molar fraction of A atoms for the entire alloy $\text{A}_x\text{B}_{1-x}\text{C}$ is fixed by x , the cluster fractions x_j have to obey the second constraint,

$$\sum_{j=0}^J n_j x_j = nx. \quad (2)$$

Using such a cluster expansion, any macroscopic alloy can be built from the microscopic clusters, each of which contributes with its cluster fraction. Consequently, within this framework each property P of the macroscopic system can be traced back to the respective properties P_j of the clusters. Given the weights $x_j(x, T)$ for an alloy of a certain composition x at a temperature T and the values P_j of the property for each cluster, one can calculate the property $P(x, T)$ for the alloy using the Connolly-Williams method,^{30,38}

$$P(x, T) = \sum_{j=0}^J x_j(x, T) P_j. \quad (3)$$

With this approach, structural, elastic, and thermodynamic properties, including lattice parameters and bulk moduli can be accessed.

Both the $\text{Mg}_x\text{Zn}_{1-x}\text{O}$ alloy and the $\text{Cd}_x\text{Zn}_{1-x}\text{O}$ alloy consist of two monoxides, which show different equilibrium lattice structures: MgO and CdO crystallize in the cubic rs phase while the equilibrium structure of ZnO is the hexagonal wz phase under ambient conditions. In this work, we follow previous argumentations^{35,39} that it is sufficient to include next-nearest-neighbor correlations to capture large parts of the physics involved in the problem. Consequently, we use 16-atom cluster cells (i.e., $n=8$) and assume that possible correlations between the different clusters are small.

While we rely on the cluster expansion for the wz structure which is described in Ref. 35, we present a new one for alloys with rs crystal structure in this work. The corresponding unit cells and the labeling of the cation positions for both types, wz and rs clusters, are illustrated in Fig. 1. In Table I, we give the number n_j of A cations, the degeneracy factors g_j , and one representative of the symmetry-equivalent clusters for each class j (characterized by the cation sites that are occupied with A atoms). The degeneracy g_j for each class as well as the total number of classes $J+1$ do not only depend on the number of atoms in the clusters but also on the actual point group of the crystal. For $n=8$, we obtain 22 classes in the wz case and 16 classes for the rs structure (see Table I). Taking into account the degeneracies g_j , a total of 256 clusters per crystal structure are studied for each pseudobinary material system.

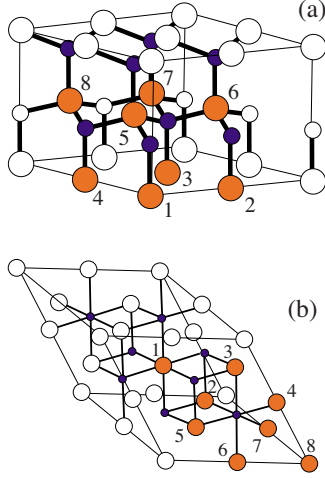


FIG. 1. (Color online) Illustration of atomic sites in the 16-atom clusters of (a) wurtzite and (b) rocksalt structure. Anions (C atoms) are depicted in blue (small), cations (A or B atoms) in red (large). White atoms represent the surrounding lattice and are not part of the 16-atom clusters. The denotation 1–8 of the cations is used in Table I.

B. Generalized quasichemical approximation

In the framework of the GQCA,^{29–32,34} the cluster fractions are determined by a minimization of the Helmholtz free

energy $F(x, T)$. We restrict the discussion to the mixing contribution ΔF to the free energy,

$$\Delta F(x, T) = \Delta U(x, T) - T\Delta S(x, T). \quad (4)$$

The mixing contribution to the internal energy $\Delta U(x, T)$ is calculated as the sum over the contributions from the M clusters and is referenced to the value of U of an alloy consisting only of the two binary end components AC and BC,

$$\begin{aligned} \Delta U(x, T) &= M \left\{ \sum_{j=0}^J x_j \varepsilon_j - [x \varepsilon_J + (1-x) \varepsilon_0] \right\} \\ &= M \sum_{j=0}^J \Delta \varepsilon_j x_j. \end{aligned} \quad (5)$$

Here we introduce the definition of the excess energy $\Delta \varepsilon_j$ for the class j ,

$$\Delta \varepsilon_j = \varepsilon_j - \left(\frac{n_j}{n} \varepsilon_J + \frac{n - n_j}{n} \varepsilon_0 \right). \quad (6)$$

For the calculation of the free energy, Eq. (4), or thermodynamic properties derived thereof, an expression for the configurational (or mixing) entropy has to be found.³⁰ To evaluate the Boltzmann definition of the entropy, $\Delta S(x, T) = k_B \ln W$, one has to give an expression for the number of

TABLE I. Cluster classes for 16-atom cells in wz and rs crystal structure. For each class j , the number n_j of A cations, the degeneracy g_j of the class and the cation sites occupied with A-type atoms (for one representative of the class) are given.

wz				rs			
j	n_j	g_j	A atoms	j	n_j	g_j	A atoms
0	0	1		22	0	1	
1	1	8	1	23	1	8	1
2	2	12	1,2	24	2	24	1,2
3	2	12	1,5	25	2	4	4,5
4	2	4	1,8	26	3	32	1,2,3
5	3	8	1,2,3	27	3	24	1,4,5
6	3	24	1,2,7	28	4	8	1,2,3,4
7	3	24	1,2,5	29	4	8	1,2,3,5
8	4	2	1,2,3,4	30	4	48	1,2,4,5
9	4	8	1,2,3,5	31	4	6	3,4,5,6
10	4	24	1,2,4,5	32	5	32	1,2,3,4,5
11	4	6	1,2,5,6	33	5	24	1,3,4,5,6
12	4	6	1,2,7,8	34	6	24	1,2,3,4,5,6
13	4	24	1,2,5,8	35	6	4	2,3,4,5,6,7
14	5	24	3,4,6,7,8	36	7	8	1,2,3,4,5,6,7
15	5	24	3,4,5,6,8	37	8	1	1,2,3,4,5,6,7,8
16	5	8	4,5,6,7,8				
17	6	4	2,3,4,5,6,7				
18	6	12	2,3,4,6,7,8				
19	6	12	3,4,5,6,7,8				
20	7	8	2,3,4,5,6,7,8				
21	8	1	1,2,3,4,5,6,7,8				

possible configurations W . Given a cluster expansion and, therefore, a set of cluster fractions $\{x_j\}$ that fulfills the constraints (1) and (2), W describes the number of possible atomic configurations in the entire alloy, i.e., W counts all possible ways of arranging the N_A A atoms and N_B B atoms for one given set $\{x_j\}$ on the $N=N_A+N_B$ cation sites. To determine W , the number of ways of arranging the M_0, M_1, \dots, M_J clusters to form the alloy, $M!/\prod_j M_j!$, has to be multiplied by the number of possibilities to arrange the cations in each cluster. Since one cluster of class j can be occupied by cations in g_j ways, all M_j clusters lead to $g_j^{M_j}$ possibilities. Taking into account all classes j one ultimately obtains

$$W = \frac{M!}{\prod_{j=0}^J M_j!} \cdot \prod_{j'=0}^J g_j^{M_{j'}}. \quad (7)$$

Using this expression for W and the definition $x_j = M_j/M$, one finds for the mixing entropy ΔS in the Stirling limit,

$$\Delta S(x, T) = -k_B M \sum_{j=0}^J x_j \ln \left(\frac{x_j}{g_j} \right). \quad (8)$$

Introducing the *ideal* cluster fractions of a strict-regular solution³⁴ (see Sec. II C),

$$x_j^0 = g_j x^{n_j} (1-x)^{n-n_j}, \quad (9)$$

the mixing entropy can be rewritten into^{30,34}

$$\Delta S(x, T) = -k_B \left\{ N[x \ln x + (1-x) \ln(1-x)] + M \sum_{j=0}^J x_j \ln \left(\frac{x_j}{x_j^0} \right) \right\}. \quad (10)$$

Although the expressions for W according to Eq. (7) and the one derived in Ref. 30 differ, Eq. (10) shows that they both lead to the same entropy in the Stirling limit.

Equations (5) and (8) fully determine the Helmholtz mixing free energy as a function of x and T , given that the cluster fractions x_j are known for x and T . In the GQCA, the x_j are determined by the requirement that $\Delta F(x, T)$ assumes a minimum with respect to the cluster distribution, i.e., $\partial \Delta F(x, T) / \partial x_j = 0$. Hence, the Lagrange formalism with the constraints (1) and (2) yields

$$x_j^{\text{GQCA}}(x, T) = \frac{g_j \eta^{n_j} e^{-\beta \Delta \varepsilon_j}}{\sum_{j'=0}^J g_{j'} \eta^{n_{j'}} e^{-\beta \Delta \varepsilon_{j'}}} \quad (11)$$

whereas $\beta = 1/k_B T$. The parameter η has to be determined from the condition that the x_j^{GQCA} obey the constraint (2). The cluster fractions x_j^{GQCA} according to Eq. (11) describe the probability for the occurrence of each cluster class j in an alloy which has been prepared under thermodynamic equilibrium conditions that minimize the free energy.

Since we study two cases, isostructural (wz or rs only) as well as heterostructural (combined wz and rs) alloys, we distinguish three situations: (i) wz clusters only, (ii) rs clusters only, or (iii) simultaneous occurrence of wz and rs clusters.

Depending on the clusters included in the calculation, the value for J has to be set to $J=21$, 15, or 37 (see Table I) and the minimization of ΔF has to be performed for given x and T accordingly, which leads, via Eq. (11), to the corresponding x_j^{GQCA} for each case.

C. Strict-regular solution and microscopic decomposition limit

In the literature, several techniques for the deposition of $\text{Mg}_x\text{Zn}_{1-x}\text{O}$ films are reported, e.g., pulsed laser deposition (PLD) with growth temperatures of 950, ..., 1050 K,¹⁰ radio-frequency magnetron sputtering at 700 K,⁴⁰ and reactive electron-beam evaporation at a substrate temperature of 550 K.²¹ Similar techniques have been applied for $\text{Cd}_x\text{Zn}_{1-x}\text{O}$ layers, however, at much lower substrate temperatures, e.g., MBE with a growth temperature as low as 450 K,¹² (plasma-enhanced) MOCVD at a growth temperature of 625 K,^{13,24} or PLD at 700 K.²³ Subsequent repeated temper steps are reported in some cases. The films are typically deposited on *c*-plane (0001) sapphire but also *a*-plane sapphire or more exotic substrates have been used. Therefore, the respective experimental situation suggests the studying of certain nonequilibrium preparation conditions, for which the actual cluster statistics may be modified by kinetic barriers, frozen high-temperature states, as well as interface or surface influences. In order to simulate a dependence of the cluster distribution on the preparation conditions we study two limiting cases:

(i) the strict-regular solution (SRS) model.³⁴ In this case, the *ideal* cluster fractions x_j^0 according to Eq. (9) are used which arise from a purely stochastic distribution of the clusters. These x_j^0 do neither depend on the temperature nor the clusters' excess energies but are only determined by x and n_j . The number W is then simply given by all possible arrangements of $N_A = xN$ A atoms and $N_B = (1-x)N$ B atoms on the $N = N_A + N_B$ cation sites of the alloy, i.e.,

$$W^{\text{SRS}} = \frac{N!}{N_A! N_B!}. \quad (12)$$

In the Stirling limit, the mixing entropy in this case reduces to

$$\Delta S^{\text{SRS}}(x) = -k_B N [x \ln x + (1-x) \ln(1-x)]. \quad (13)$$

The ideal x_j^0 according to Eq. (9) and ΔS^{SRS} can be interpreted as the high-temperature limit of the GQCA since for increasing temperatures, the x_j^{GQCA} approach the x_j^0 and, consequently, ΔS [cf. Eq. (8)] approaches ΔS^{SRS} .

(ii) The microscopic decomposition model (MDM). In this limiting case, the cations of type A (B) are more likely to occur close to cations of type A (B). Consequently, only the clusters representing the two binary components AC and BC are allowed, with xM being the number of AC clusters and $(1-x)M$ the number of BC clusters. This is equivalent to merely a linear interpolation between the binary end components and, therefore, the results are equal to predictions from Vegard's rule.^{30,41} Furthermore, for positive excess energies $\Delta \varepsilon_j$ [cf. Eq. (6)], the x_j^{MDM} represent the low-temperature limit of the GQCA. The cluster fractions for the MDM are given by

$$x_j^{\text{MDM}} = \begin{cases} 1-x & \text{for } j=0 \\ x & \text{for } j=J \\ 0 & \text{otherwise.} \end{cases} \quad (14)$$

The number of atomic configurations follows immediately from Eq. (7) by taking into account only the two clusters with $j=0$ and $j=J$, i.e.,

$$W^{\text{MDM}} = \frac{M!}{[xM]![(1-x)M]!}. \quad (15)$$

Using the x_j^{MDM} , we obtain for the mixing entropy

$$\begin{aligned} \Delta S^{\text{MDM}}(x) &= -k_B M [x \ln x + (1-x) \ln(1-x)] \\ &= -\frac{1}{n} \Delta S^{\text{SRS}}(x), \end{aligned} \quad (16)$$

i.e., a reduced configurational entropy. In the MDM, the resulting length scale of decomposition of the alloy into the binary compounds is not well defined as usual in a thermodynamic approach. The minimum length scale is given by the assumed cluster size itself. Whether clusters of the same type (AC or BC) build larger regions of pure AC and BC material on a mesoscopic or macroscopic length scale depends on the cluster interaction (which is not taken into account). In general, the MDM describes alloys that have been prepared under conditions where mixing does not lead to a gain of internal energy. Indeed, in the MDM description one finds from Eq. (5) $\Delta U(x)=0$ for the mixing contribution to the internal energy.

III. QUANTUM-MECHANICAL CALCULATIONS OF CLUSTERS

A. Computational methods

The statistical methods introduced in Sec. II trace the properties of an alloy of composition x at temperature T back to the corresponding properties of individual clusters using Eq. (3). Therefore, the respective calculations have to be performed for each of the 22 (wz) and 16 (rs) clusters of $\text{Mg}_x\text{Zn}_{1-x}\text{O}$ and $\text{Cd}_x\text{Zn}_{1-x}\text{O}$.

Ground-state properties, such as the total energy of a cluster or its structural properties, are well described within density-functional theory^{42,43} applying the supercell method, where a cluster is identified with the unit cell of an artificial crystal. Explicit calculations are performed using the Vienna *ab initio* simulation package (VASP).⁴⁴ For the semilocal generalized-gradient approximation (GGA) to the exchange and correlation (XC) potential in the Kohn-Sham equation,⁴³ we rely on the PW91 parametrization as suggested by Perdew and Wang.^{45,46} Although such a semilocal treatment of XC cannot correctly describe excitation properties (such as quasiparticle energies or excitonic effects^{47,48}), it allows for a very good description of lattice constants and cohesive energies. For the oxides studied in this work, the GGA tends to slightly underestimate binding energies and slightly overestimate lattice constants.¹⁵ However, these ground-state properties are not systematically improved by a different treat-

ment of XC, for instance, by adding an additional on-site Hubbard interaction U (Ref. 49) or a certain amount of Fock exchange.⁵⁰

The electron-ion interaction is modeled within the projector-augmented wave method.^{51,52} We treat the Mg $2p$ and Mg $3s$ as well as the O $2s$ and O $2p$ electrons as valence electrons. For Zn and Cd, the Zn $3d$ and Cd $4d$ states have to be included as valence states, respectively, together with the Zn $4s$ and Cd $5s$ electrons. The electronic wave functions are expanded into plane waves up to a cutoff energy of 450 eV and the Brillouin zone is sampled by $2 \times 2 \times 2$ (wz) or $4 \times 4 \times 4$ (rs) Monkhorst-Pack \mathbf{k} points.⁵³ We checked that these parameters give results for the total energies of the clusters that are converged within 0.08%. This corresponds to a very small level of inaccuracy, especially since the total energies of the different binary end components differ by at least 10% of their total energy.

In order to obtain the equilibrium values for the cell volumes, total energies, and bulk moduli, we minimize the total energy for several cell volumes and fit the resulting volume dependence of the total energy to the Murnaghan equation of state.⁵⁴ For each cluster geometry, we compute fully relaxed atomic positions, i.e., optimized lattice constants and internal cell parameters, ensuring that the forces acting on the ions are well below 5 meV/Å.

B. Results

To describe the geometry of the two different crystal structures on the same footing, we discuss the average cation-cation (second-nearest neighbor) distance d_2 . The results for the cluster energies ε_j , the cation-cation distances $d_{2,j}$ (averaged over all cation-cation distances of one cluster), the wz lattice parameters c_j of the cluster cell and u_j (averaged over all u 's of one cluster), the cell volumes V_j , and the bulk moduli $B_{0,j}$ are listed in Table II for all wz cluster cells and Table III for all cluster classes of the rs crystal structure.

The energies of the clusters ε_j in Tables II and III show an almost linear variation with the number n_j of Mg (Cd) atoms, decreasing (increasing) from pure ZnO to pure MgO (CdO). Small negative (positive) nonlinear deviations appear for $\text{Mg}_{n_j}\text{Zn}_{8-n_j}\text{O}_8$ ($\text{Cd}_{n_j}\text{Zn}_{8-n_j}\text{O}_8$) with absolute values of a few millielectron volt (tens of an electron volt).

The cation-cation distances $d_{2,j}$ show a weak decrease (strong increase) with the number n_j of Mg (Cd) atoms as expected from the corresponding values for the binary end components. While the nearest-neighbor distances or bond lengths (not listed in Tables II and III) of the ZnO-MgO system decrease only very slightly from $d_{\text{Zn-O}} \approx 2.002/2.167$ Å to $d_{\text{Mg-O}} \approx 1.997/2.128$ Å for wz/rs, we find a completely different situation for the ZnO-CdO system, where the bond lengths $d_{\text{Cd-O}} \approx 2.230/2.388$ Å are rather different from $d_{\text{Zn-O}}$. For the bulk moduli $B_{0,j}$, we observe a decrease with increasing number n_j of Mg or Cd atoms, independent of the crystal structure. This trend follows the behavior of the covalent radii of the cations that also show an anomalous trend of 1.36, 1.25, and 1.48 Å along the row Mg, Zn, and Cd.⁵⁵ For our calculated lattice

TABLE II. Cluster energies per cation-anion pair ε_j , cation-cation distances $d_{2,j}$, lattice parameters c_j and u_j , volume per cation-anion pair V_j , and bulk moduli $B_{0,j}$ for 16-atom clusters of $\text{Mg}_{n_j}\text{Zn}_{8-n_j}\text{O}_8$ (first line of each class) and $\text{Cd}_{n_j}\text{Zn}_{8-n_j}\text{O}_8$ (second line of each class) in wz structure.

Class j	ε_j (eV/pair)	$d_{2,j}$ (Å)	c_j (Å)	u_j	V_j (Å ³)	$B_{0,j}$ (GPa)
0	-9.05	3.270	5.303	0.378	24.72	141.0
1	-9.41	3.268	5.288	0.380	24.68	137.5
	-8.87	3.315	5.368	0.379	25.75	121.3
2	-9.76	3.270	5.275	0.381	24.73	131.6
	-8.69	3.359	5.452	0.378	26.80	110.2
3	-9.76	3.266	5.275	0.381	24.64	131.3
	-8.70	3.357	5.405	0.382	26.74	112.7
4	-9.76	3.266	5.271	0.381	24.64	131.1
	-8.71	3.358	5.445	0.379	26.77	112.5
5	-10.12	3.265	5.243	0.383	24.61	121.5
	-8.51	3.408	5.565	0.374	27.98	114.2
6	-10.12	3.265	5.252	0.382	24.60	121.6
	-8.55	3.405	5.508	0.380	27.91	117.2
7	-10.12	3.265	5.260	0.382	24.60	121.4
	-8.54	3.404	5.459	0.384	27.87	116.0
8	-10.47	3.264	5.211	0.385	24.57	118.4
	-8.33	3.455	5.705	0.368	29.16	103.7
9	-10.47	3.264	5.235	0.384	24.58	118.1
	-8.37	3.451	5.542	0.383	29.03	104.0
10	-10.47	3.264	5.232	0.384	24.57	118.0
	-8.38	3.452	5.591	0.378	29.07	105.9
11	-10.47	3.264	5.246	0.383	24.58	117.3
	-8.39	3.447	5.467	0.390	28.89	104.1
12	-10.47	3.263	5.233	0.384	24.57	118.8
	-8.41	3.450	5.583	0.380	29.03	107.6
13	-10.47	3.264	5.241	0.383	24.57	117.6
	-8.40	3.449	5.531	0.384	28.98	105.1
14	-10.82	3.261	5.216	0.385	24.52	116.8
	-8.24	3.495	5.576	0.387	30.13	95.9
15	-10.82	3.261	5.210	0.385	24.51	116.7
	-8.25	3.497	5.636	0.381	30.22	98.2
16	-10.82	3.262	5.198	0.386	24.53	114.7
	-8.21	3.501	5.711	0.374	30.33	96.3
17	-11.17	3.260	5.183	0.387	24.48	113.2
	-8.11	3.544	5.714	0.382	31.48	98.4
18	-11.17	3.260	5.191	0.387	24.49	110.3
	-8.10	3.542	5.647	0.387	31.38	96.6
19	-11.17	3.261	5.182	0.387	24.50	109.8
	-8.08	3.546	5.727	0.380	31.51	96.0
20	-11.52	3.259	5.158	0.389	24.46	110.5
	-7.95	3.592	5.762	0.384	32.74	92.4
21	-11.86	3.258	5.120	0.391	24.41	104.4
	-7.82	3.640	5.841	0.384	34.10	90.6

parameters, equilibrium volumes, and bond lengths, we find very good agreement with a similar study.³⁶ However, the deviations are remarkable for the total energies and, consequently, lead to different results for, e.g., the mixing free

energy. We attribute these differences to the use of the local-density approximation (LDA) to XC, and to the neglect of the Zn 3*d* and Cd 4*d* electrons as valence electrons in Ref. 36.

TABLE III. Cluster energies per cation-anion pair ϵ_j , cation-cation distances $d_{2,j}$, volume per cation-anion pair V_j , and bulk moduli $B_{0,j}$ for 16-atom clusters of $\text{Mg}_n\text{Zn}_{8-n}\text{O}_8$ (first line of each class) and $\text{Cd}_n\text{Zn}_{8-n}\text{O}_8$ (second line of each class) in rs structure.

Class j	ϵ_j (eV/pair)	$d_{2,j}$ (Å)	V_j (Å ³)	$B_{0,j}$ (GPa)
0	-8.75	3.065	20.36	166.3
1	-9.16	3.059	20.23	165.4
	-8.57	3.111	21.29	162.1
2	-9.57	3.052	20.09	162.7
	-8.42	3.152	22.14	154.9
3	-9.57	3.053	20.11	162.9
	-8.34	3.165	22.43	155.4
4	-9.98	3.044	19.95	160.9
	-8.31	3.189	22.92	147.5
5	-9.98	3.045	19.97	155.0
	-8.24	3.202	23.21	147.3
6	-10.39	3.037	19.81	158.5
	-8.22	3.224	23.69	144.9
7	-10.39	3.037	19.80	158.7
	-8.22	3.224	23.70	144.9
8	-10.39	3.038	19.83	159.0
	-8.15	3.236	23.95	145.0
9	-10.39	3.039	19.85	159.2
	-8.09	3.247	24.22	144.3
10	-10.80	3.030	19.67	156.7
	-8.09	3.267	24.66	138.4
11	-10.80	3.031	19.70	139.5
	-8.03	3.280	24.95	132.5
12	-11.20	3.023	19.54	156.3
	-7.99	3.315	25.75	114.1
13	-11.21	3.024	19.56	157.4
	-8.00	3.344	26.39	101.8
14	-11.61	3.016	19.40	153.5
	-7.90	3.343	26.42	130.8
15	-12.01	3.009	19.26	152.0
	-7.84	3.378	27.25	126.9

IV. THERMODYNAMIC PROPERTIES

By including the temperature-dependent mixing entropy, we also obtain a temperature dependence of the cluster fractions and, therefore, of the derived properties. In this work, we discuss the alloy properties at two selected temperatures, (i) room temperature ($T=300$ K) where many measurements are performed and (ii) an exemplary growth temperature of $T=1100$ K.

A. Excess energies

The excess energy [cf. Eq. (6)] $\Delta\epsilon_j$ represents the energy of formation of a certain $X_n\text{Zn}_{8-n}\text{O}_8$ cluster in the wz or rs structure with respect to ZnO and XO ($X=\text{Mg}$ and Cd) in the

respective crystal structure. They are fundamental quantities for the GQCA since they ultimately determine the cluster fractions [see Eq. (11)] and, therefore, the alloy statistics. In Fig. 2, the excess energies are plotted for both material combinations, i.e., ZnO-MgO and ZnO-CdO. Whereas in Figs. 2(a) and 2(b), the $\Delta\epsilon_j$ for wz and rs structure are shown, we visualize the energetic difference of these two lattice structures by plotting the $\Delta\epsilon_j$ using the value of ϵ_0 for wz-ZnO and ϵ_j for rs-XO in Figs. 2(c) and 2(d).

For MgZnO clusters [cf. Fig. 2(a)], we find negative excess energies (per anion-cation pair) with absolute values of less than 20 meV for both crystal structures. Contrary, for CdZnO clusters [cf. Fig. 2(b)] the excess energies are positive for both polymorphs and by one order of magnitude larger than the ones for MgZnO. As a consequence, in the isostructural limit with *only* a fourfold (wz) or a sixfold (rs) coordinated bonding configuration, we predict that mixing is possible for the ZnO-MgO system independent of the composition x , temperature T , and the boundary condition that fixes the cluster fractions. In the case of the ZnO-CdO system with its large difference of the bond lengths $d_{\text{Zn-O}}/d_{\text{Cd-O}}$ and, hence, a remarkable strain of a bond in the environment of the other cation species, the situation is different and will be discussed in detail in Sec. IV C

Due to the changed reference energy of the excess energies in Fig. 2(c) and their small absolute values in the case of ZnO-MgO, we find an almost linear variation between the end points. The crossing point near $n_j/n \approx 2/3$ indicates that for small Mg fractions, the fourfold coordination is more stable while for larger Mg fractions, the sixfold one seems to be energetically favored. This is in agreement with the occurrence of the cubic crystal structure above a composition of $x \approx 0.67$ in PLD samples.¹⁸ However, there are also experimental²¹ or other theoretical results^{16,36,37} contradicting our findings. More precisely, Refs. 16 and 36 find for rs-ZnO and wz-ZnO almost the same energy difference as we do for rs-MgO and wz-MgO and vice versa. There are strong indications that the use of the LDA instead of the GGA can cause such deviations of the total-energy differences. Our presumption is supported by a comparison to other GGA calculations that confirm our result of 0.3 eV as the energy difference between rs-ZnO and wz-ZnO as well as the 0.15 eV between rs-MgO and wz-MgO.^{56,57} LDA values that have been reported seem to lead to opposite differences for MgO and ZnO.^{16,36,37,58,59} In addition, Fan *et al.*³⁶ do not include the d electrons of Zn or Cd in their calculations which may further influence the rs-wz splittings.

We observe a different situation for the ZnO-CdO system [cf. Fig. 2(d)] since the absolute values of the excess energies are comparable to the energy differences of the rs and wz polymorphs. Consequently, the deviations from the linear interpolation between the end components are much larger. Furthermore, the wz and rs polymorphs of CdO are energetically much closer to each other than the corresponding ZnO polymorphs. Merely plotting the excess energies [see Fig. 2(d)] suggests a wide range up to $n_j/n \approx 0.95$ for the stability of wz which contradicts the majority of experiments.^{12,13,23,24,60} Taking the cluster statistics into account, we discuss this issue in more detail later [cf. Secs. IV C and IV D].

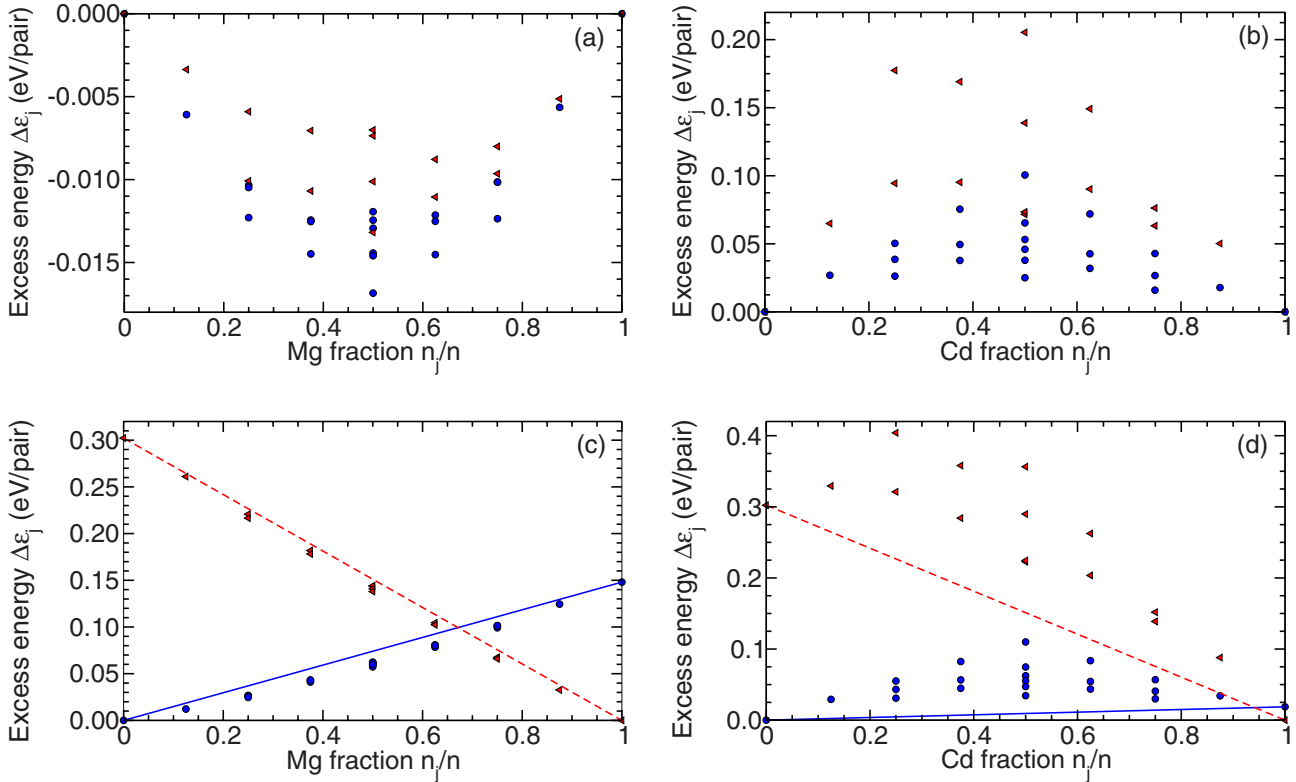


FIG. 2. (Color online) Excess energies per cation-anion pair $\Delta\varepsilon_j$ of the [(a) and (c)] $\text{Mg}_{n_j}\text{Zn}_{n-n_j}\text{O}_{n_j}$ and [(b) and (d)] $\text{Cd}_{n_j}\text{Zn}_{n-n_j}\text{O}_{n_j}$ clusters computed from Eq. (6). The excess energies are shown for the rocksalt (red triangles) and the wurtzite (blue circles) crystal structures. In subfigures (a) and (b) [subfigures (c) and (d)], the ε_0 and ε_j of the same crystal structure [equilibrium crystal structure] have been used as level of reference. The lines linearly connect the end points wz-ZnO and wz-XO (solid blue) as well as rs-ZnO and rs-XO (dashed red), $X=\text{Mg}$ and Cd .

B. Internal energy and entropy

For a general discussion of the thermodynamic trends resulting from the three different statistics, we compare the contributions ΔU [Eq. (5)] and ΔS [Eq. (10)] to the mixing free energy ΔF as calculated from the GQCA with results obtained using the ideal weights and the weights from the MDM for wz- $\text{Mg}_x\text{Zn}_{1-x}\text{O}$.

From the mixing contribution to the internal energy $\Delta U(x, T)$ of wz- $\text{Mg}_x\text{Zn}_{1-x}\text{O}$, it can be seen [cf. Fig. 3(a)] that for low temperatures ($T=30$ K) only the clusters with the lowest energies contribute in the GQCA. For higher temperatures ($T=300$ K), the weights of clusters with higher excess energies are larger. The SRS model finally represents the high-temperature limit of the GQCA in which all wz clusters contribute. The MDM does not lower the internal energy of the system.

In Fig. 3(b), the corresponding results for the mixing entropy $\Delta S(x, T)$ are shown. Again, the MDM is the most trivial case with the smallest entropy term since only two clusters contribute. The SRS model is obviously maximizing the entropy which is consistent with what we expect from a high-temperature limit, i.e., the high-temperature curve of the GQCA approaches the SRS limit. The low-temperature curve of the GQCA shows an interesting behavior since the entropy in this case clearly features pronounced minima for compositions x where only single clusters substantially contribute.

C. Mixing free energy

The Gibbs free energy is the thermodynamic potential which describes the equilibrium of a system for fixed tem-

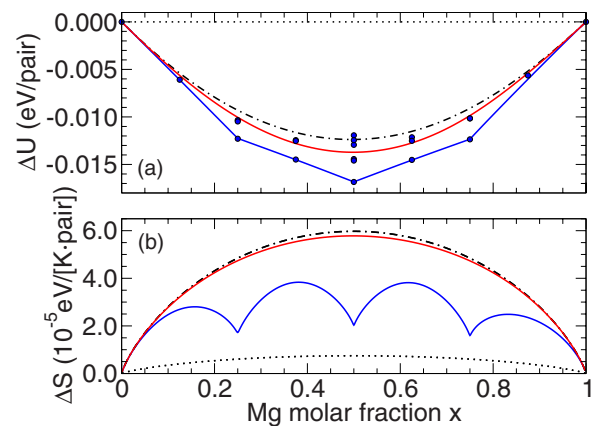


FIG. 3. (Color online) Mixing contribution to the (a) internal energy $\Delta U(x, T)$ and (b) mixing entropy $\Delta S(x, T)$ for $\text{Mg}_x\text{Zn}_{1-x}\text{O}$ in wz structure. The solid curves are obtained using the GQCA cluster fractions for $T=30$ K (blue) and $T=300$ K (red). The dotted curves result from the MDM and the dashed-dotted curves are obtained using the ideal cluster fractions. For comparison, the blue dots represent the excess energies computed from Eq. (6). All quantities are normalized to cation-anion pairs.

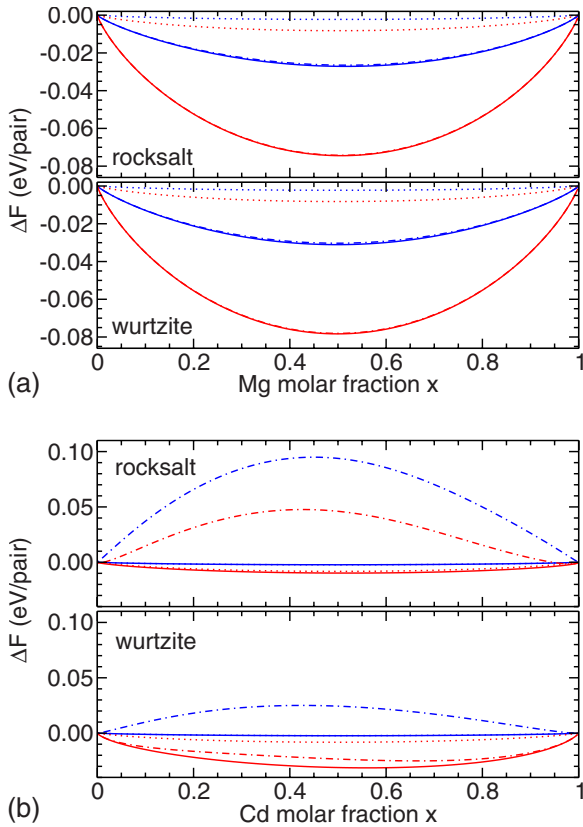


FIG. 4. (Color online) Mixing free energy $\Delta F(x, T)$ of (a) $\text{Mg}_x\text{Zn}_{1-x}\text{O}$ and (b) $\text{Cd}_x\text{Zn}_{1-x}\text{O}$ alloys with fixed sixfold (rs) or fourfold (wz) bonding configuration versus composition x . The solid curves are obtained using cluster fractions from the GQCA. The dotted curves result from the MDM and the dashed-dotted curves are obtained using the ideal cluster fractions. In each case, we depict results for $T=300$ K (blue curves) and $T=1100$ K (red curves).

perature and pressure. At low pressures of about 1 atm, the difference between the Gibbs free energy and the Helmholtz free energy vanishes. Therefore, the Helmholtz mixing free energy is used as the central thermodynamic quantity that governs, at least for solids and low pressures, the equilibrium alloy state and, therefore, the cluster fractions x_j^{GQCA} .

In Fig. 4, the mixing free energy $\Delta F(x, T)$ for $\text{Mg}_x\text{Zn}_{1-x}\text{O}$ and $\text{Cd}_x\text{Zn}_{1-x}\text{O}$ alloys in the wz and the rs crystal structures is plotted versus composition x . For $\text{Mg}_x\text{Zn}_{1-x}\text{O}$, it is obvious that $\Delta F < 0$ for all x and T , which is, according to Eqs. (4) and (5), a direct consequence of the negative excess energies for $\text{Mg}_n\text{Zn}_{n-n_i}\text{O}_n$ clusters [cf. Fig. 2(a)]. For that reason, all three statistics agree in predicting wz- $\text{Mg}_x\text{Zn}_{1-x}\text{O}$ and rs- $\text{Mg}_x\text{Zn}_{1-x}\text{O}$ to be a random alloy without a miscibility gap,³⁴ independent of x and T . There is no tendency for binodal or spinodal decomposition of the alloy. The results using the GQCA cluster weights and the ones from the SRS model are almost identical while the energy gain is smaller within the MDM.

For $\text{Cd}_x\text{Zn}_{1-x}\text{O}$, the behavior of ΔF is qualitatively different as can be seen from Fig. 4(b). It shows that for $T=300$ K and both crystal structures, the GQCA results agree very well with the MDM, i.e., we find the alloy being almost

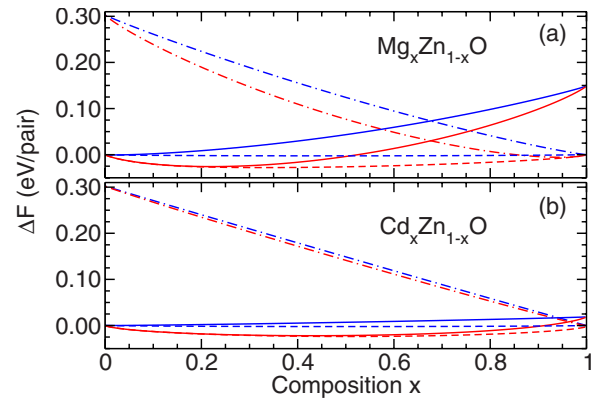


FIG. 5. (Color online) Mixing free energy $\Delta F(x, T)$ of (a) $\text{Mg}_x\text{Zn}_{1-x}\text{O}$ and (b) $\text{Cd}_x\text{Zn}_{1-x}\text{O}$ alloys versus composition x . The curves are obtained using the GQCA with wurtzite clusters only (solid), rocksalt clusters only (dashed-dotted), or both types of clusters (dashed). In all cases, results are shown for $T=300$ K (blue curves) and $T=1100$ K (red curves). The equilibrium crystal structures wz ($x=0$) and rs ($x=1$) have been used as energy zero.

entirely decomposed into the binary clusters. For the higher temperature of $T=1100$ K, the GQCA result approaches the SRS curve for the wurtzitic alloy, especially for $x < 0.1$ and $x > 0.8$. However, for rs- $\text{Cd}_x\text{Zn}_{1-x}\text{O}$ at $T=1100$ K, the GQCA curve still agrees with the MDM. In this case, the system has a strong tendency for decomposition into the binary materials and the SRS limit can only be reached at very high temperatures. Besides, for $\text{Cd}_x\text{Zn}_{1-x}\text{O}$, the ΔF curves versus x are rather asymmetric for the SRS and show minima and inflection points with positions that strongly depend on the temperature and the local crystal structure. This is an indication of a phase transition between random and phase-separated alloys and will be discussed as such later.

In the following, we compare to free-energy curves that are computed using the energies of the respective *equilibrium* crystal structures (rs-MgO, wz-ZnO, and rs-MgO) as level of reference, in contrast to the results in Fig. 4 where the energies of the binary components in the same crystal structure have been used. For $\text{Mg}_x\text{Zn}_{1-x}\text{O}$, the mixing free-energy curves for the wz alloys and the rs alloys in Fig. 5(a) intersect at $x \approx 0.67$, independent of the temperature. We interpret this as a tendency for a transition from preferred fourfold coordination (wz) to preferred sixfold coordination (rs) at that composition under equilibrium conditions. In addition, the difference of the mixing free energy per cluster of the heterostructural alloys and that of the respective isostructural cases exceeds 25 meV, i.e., $k_B T$ at room temperature, for approximately $0.10 \leq x \leq 0.98$ ($0.28 \leq x \leq 0.93$) at $T=300$ K ($T=1100$ K). The additional degree of freedom of varying also the atomic coordination leads to the lowest mixing free energy [see Fig. 5(a)]. Hence, for these values of x both, rs as well as wz clusters, significantly contribute to the alloy material.

The same tendencies have been observed in experimental studies. Minemoto *et al.*⁶¹ (Vashaei *et al.*⁶²) found predominantly wz structure below $x \leq 0.46$ ($x \leq 0.34$) and mainly rs structure for $x \geq 0.62$ ($0.65 \leq x \leq 0.97$). Ohtomo *et al.*⁶³ report on the occurrence of an impurity phase above Mg con-

centrations of $x \approx 0.33$ which roughly coincides with the point in Fig. 5(a) where the high-temperature curve for wz structure starts to deviate from the curve for the mixed statistics. Also the x-ray diffraction measurements of thin-film samples by Bundesmann *et al.*¹⁸ reveal hexagonal wz structure for $x \leq 0.53$ and cubic rs structure for $x \geq 0.67$. Films grown by reactive electron-beam evaporation²¹ lead to hexagonal $\text{Mg}_x\text{Zn}_{1-x}\text{O}$ up to $x=0.51$ and to cubic $\text{Mg}_x\text{Zn}_{1-x}\text{O}$ above $x=0.55$. In general, the amount of fourfold- or sixfold-coordinated atoms cannot be directly derived from the mixing free energy and will be discussed in more detail in Sec. IV D

In the case of the $\text{Cd}_x\text{Zn}_{1-x}\text{O}$ alloys, we study the mixing free energy in Fig. 5(b) where we observe a crossing of the curves for the isostructural alloys roughly at a Cd content of $x \approx 0.95$. Moreover, we find that the result from the mixed statistics differs less than 25 meV (per cluster) from the curve for the pure wz structure up to compositions x of about 0.17 (0.59) for $T=300$ K ($T=1100$ K). The reason for that behavior is the small energy difference between the rs-CdO and the wz-CdO phase¹⁵ (see Tables II and III).

Experimental studies of $\text{Cd}_x\text{Zn}_{1-x}\text{O}$ show an ambivalent picture while two groups report very low thermodynamic solubility limits²³ of only $x \approx 0.07$ or phase separation at even lower Cd concentrations,²⁴ another group observed Cd concentrations up to $x=0.32$ in samples produced by means of highly nonequilibrium MBE.¹² Unfortunately, they have not tried for higher concentrations. More importantly, the wz crystal structure has also been found for plasma-enhanced MOCVD layers¹³ up to $x=0.697$. Their result is confirmed by Ishihara *et al.*⁶⁰ who report a transition from wz to rs structure at $x=0.7$ for films deposited by MOCVD. Apparently, the change in the crystal structure occurs at lower Cd concentrations than we predicted from the intersection of the ΔF curves for wz and rs in Fig. 5(b). On the other hand, the high-temperature curve from the mixed statistics shows significant deviations from the pure wz statistics above Cd contents of about 0.7 which may explain the experimental findings.⁶⁰

For a detailed discussion of the mixed statistics we present in Fig. 6 the results for the mixing free energy obtained from the statistics with wz and rs clusters. In this plot, we use again the equilibrium crystal structures for each material as level of reference for the mixing free energies at $x=0$ and $x=1$. Since the ideal cluster fractions x_j^0 according to Eq. (9) do not depend on the cluster energies, both the sum of the x_j^0 for all wz clusters and also of all rs clusters give the same total weight of 0.5. Consequently, at $x=0$ and $x=1$ clusters of both crystal structures contribute equally, albeit, we want to take this situation into account due to possible nonequilibrium growth conditions. Therefore, we set the mixing free energies at $x=0$ and $x=1$ to zero for each curve resulting from the SRS model in Fig. 6 since otherwise, $\Delta F(x=0, T) > 0$ and $\Delta F(x=1, T) > 0$ hold for temperatures $T > 0$ K due to the weights of the SRS model.

First of all, Fig. 6 points out that the GQCA and the MDM coincide for both materials at low temperatures. Contrary, the SRS model and the GQCA result in a remarkable difference independent of the temperature. This is not surprising since the SRS model neglects the large energetic differences be-

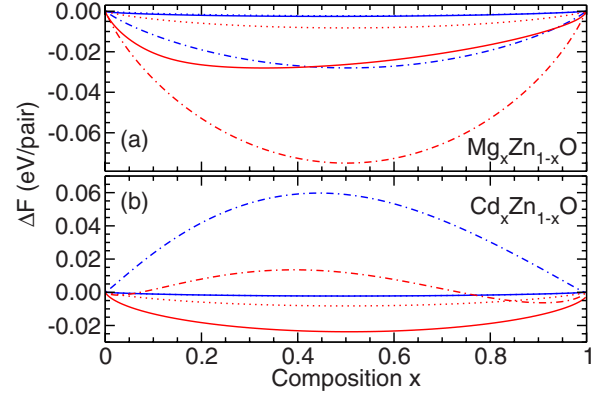


FIG. 6. (Color online) Mixing free energy $\Delta F(x, T)$ of (a) $\text{Mg}_x\text{Zn}_{1-x}\text{O}$ and (b) $\text{Cd}_x\text{Zn}_{1-x}\text{O}$ alloys versus composition x for $T=300$ K (blue) and $T=1100$ K (red). The solid curves are computed using cluster fractions from the GQCA. The dotted curves are obtained for the MDM while the dashed-dotted curves are calculated using the ideal cluster fractions. All curves result from the combined statistics with both wurtzite- and rocksalt-type clusters. The respective composition end points have been used as zero (see text).

tween the two crystal structures by merely assigning the ideal weights to the clusters. While we find for $\text{Mg}_x\text{Zn}_{1-x}\text{O}$, which shows negative excess energies, that the ideal cluster fractions are energetically favored over the ones resulting from GQCA or the MDM [cf. Fig. 6(a)], the opposite is true for $\text{Cd}_x\text{Zn}_{1-x}\text{O}$ [cf. Fig. 6(b)], where the excess energies are positive.

D. Phase transitions and phase diagram

For a better understanding of the structural composition of the alloys as a function of x and T , we calculate the contributions of wz and rs clusters to the mixed statistics results. For that purpose we define the wz character x^{wz} and the rs character x^{rs} of the alloy as the sum over the corresponding weights, i.e.,

$$x^{\text{wz}} = \sum_{j=0}^{21} x_j \quad \text{and} \quad x^{\text{rs}} = \sum_{j=22}^{37} x_j, \quad (17)$$

with $x^{\text{wz}} + x^{\text{rs}} = 1$. For given composition x , temperature T , and statistical model x^{wz} (x^{rs}) measures the relative contribution of clusters with fourfold (sixfold) atomic coordination to the studied (nondecomposed) $X_x\text{Zn}_{1-x}\text{O}$ sample ($X=\text{Mg}$ and Cd). The results for x^{wz} and x^{rs} as a function of x and T are shown for both pseudobinary materials in Fig. 7. This figure clarifies how the dominating crystal structure in the alloy depends on the thermodynamic conditions as well as the respective cluster statistics (GQCA, SRS, and MDM). As discussed before, the SRS model for the cluster fractions gives rise to equal contributions of rs and wz clusters (see Fig. 7). We confirm our discussion of the results for the mixing free energy by finding the GQCA curves close to the MDM results for both materials at room temperature. As expected, higher preparation temperatures tend to move the intersection $x^{\text{wz}} = x^{\text{rs}}$ to larger Mg or Cd molar fractions x . More

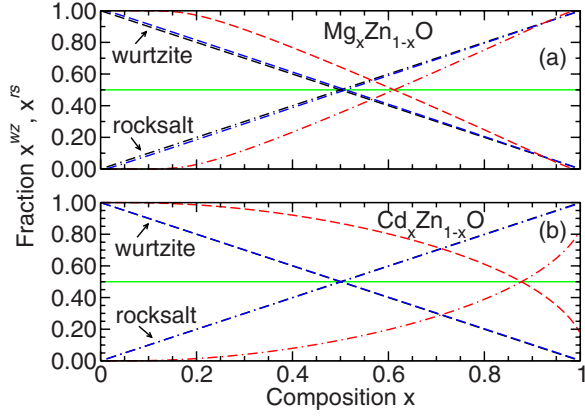


FIG. 7. (Color online) Crystal-structure fractions x^{wz} (dashed curves) and x^{rs} (dashed-dotted curves) of $\text{Mg}_x\text{Zn}_{1-x}\text{O}$ (a) and $\text{Cd}_x\text{Zn}_{1-x}\text{O}$ (b) alloys versus composition x . We calculated the curves using the cluster fractions from the GQCA for $T=300$ K (blue curves) and $T=1100$ K (red curves). The solid green lines are obtained using the ideal cluster fractions. For comparison, the black curves show the result from the MDM for both crystal structures.

specifically, we find that point at about $x=0.5$ ($T=300$ K) and $x=0.6$ ($T=1100$ K) for $\text{Mg}_x\text{Zn}_{1-x}\text{O}$ while the temperature dependence is more pronounced for $\text{Cd}_x\text{Zn}_{1-x}\text{O}$ where the intersection for $T=1100$ K occurs at about $x \approx 0.87$. Consequently, the local crystal structure and bonding configuration of the $\text{Cd}_x\text{Zn}_{1-x}\text{O}$ alloy depends much more on the actual growing conditions which explains the ambivalent experimental findings for that material system.^{12,13,23,24,60}

As discussed before, the occurrence of two pronounced minima as well as inflection points in the curve for the mixing free energy of $\text{Cd}_x\text{Zn}_{1-x}\text{O}$ obtained from the SRS model (cf. Fig. 6) is an indication for a possible phase separation.²⁹ Due to its negative excess energies [cf. Fig. 2(a)], the $\text{Mg}_x\text{Zn}_{1-x}\text{O}$ alloy does not show such a behavior. To study the consequences we construct the common tangent line to the free-energy curves obtained from the SRS model for $\text{Cd}_x\text{Zn}_{1-x}\text{O}$ alloys at several T . The resulting tangent points $x_1=x_1(T)$ and $x_2=x_2(T)$ describe the boundaries of the miscibility gap and their variation with the temperature defines the binodal line in the T - x phase diagram shown in Fig. 8. From the maximum of the resulting T - x curves, we find the critical parameters $T_{\text{crit}}=1030$ K and $x_{\text{crit}}=0.34$ for the wz statistics as well as $T_{\text{crit}}=1940$ K and $x_{\text{crit}}=0.4$ for the mixed statistics. For the pure rs statistics, the critical temperature is larger than 2500 K. Inside the miscibility gap, the alloy consists of a mixture of $\text{Cd}_{x_1}\text{Zn}_{1-x_1}\text{O}$ and $\text{Cd}_{x_2}\text{Zn}_{1-x_2}\text{O}$ with the mixing free energy,

$$\Delta F_{\text{mix}}(x, T) = \frac{x_2 - x}{x_2 - x_1} \Delta F(x_1, T) + \frac{x - x_1}{x_2 - x_1} \Delta F(x_2, T), \quad (18)$$

which is lower than $\Delta F(x, T)$.

Furthermore, the two inflection points $x'_1=x'_1(T)$ and $x'_2=x'_2(T)$ of the $\Delta F(x, T)$ curve from the SRS model for $\text{Cd}_x\text{Zn}_{1-x}\text{O}$ [cf. Fig. 6(b)] define the spinodal curve in the phase diagram in Fig. 8. Inside the intervals $x_1 < x < x'_1$ and $x'_2 < x < x_2$, the alloy is metastable against local decomposi-

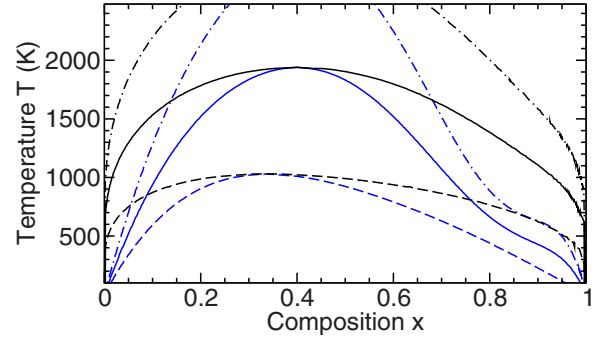


FIG. 8. (Color online) Phase diagram computed for $\text{Cd}_x\text{Zn}_{1-x}\text{O}$ using the SRS model for the cluster statistics. We show binodal (black) and spinodal (blue) curves for wz clusters only (dashed curves), rs clusters only (dashed-dotted curves), as well as for the mixed statistics including both sixfold and fourfold atomic coordination (solid curves).

tion due to an energy barrier. Contrary, spontaneous decomposition into two alloys with compositions x_1 and x_2 happens within the interval $x'_1 < x < x'_2$.²⁹ The actual distribution of the clusters depends via $x_1(T)$ and $x_2(T)$ on the composition x and temperature T (cf. Fig. 8).

The phase diagram in Fig. 8 suggests the speculation that the low solubilities of rs-CdO in wz-ZnO (Refs. 23 and 24) can be explained within the SRS model. For alloy preparation conditions that lead to a stochastic occupation of the cation lattice sites, Fig. 8 confirms a large miscibility gap starting at $x \approx 0.08$ at $T \approx 830$ K (wz clusters only), $T \approx 1450$ K (rs and wz clusters), or $T \approx 2070$ K (rs clusters only).

E. Cohesive energies

From the cluster energies ε_j as given in Tables II and III, we compute the cohesive energies (per cation-anion pair) by subtracting the total energies of the spin-polarized atoms, ε_{Mg} , ε_{Zn} , ε_{Cd} , and ε_{O} , from the ground-state energy ε_j of the j th cluster, i.e.,

$$E_{\text{coh},j} = -\varepsilon_j + \frac{n_j}{8} \varepsilon_X + \frac{n-n_j}{8} \varepsilon_{\text{Zn}} + \varepsilon_{\text{O}} \quad (19)$$

with $X=\text{Mg}$ and Cd . For the binary end components, this leads to cohesive energies of $E_{\text{coh}}=10.18$ eV (rs-MgO), 7.21 eV (wz-ZnO), and 6.00 eV (rs-CdO) which are close to experimental values of 10.26, 7.52, and 6.40 eV (see compilation in Ref. 15). In Fig. 9, the averaged cohesive energies [cf. Eq. (3)] per cation-anion pair, as computed using the cluster weights from the different statistics, are plotted for $\text{Mg}_x\text{Zn}_{1-x}\text{O}$ and $\text{Cd}_x\text{Zn}_{1-x}\text{O}$ alloys versus composition x . From Fig. 9(a), it immediately becomes clear that for $\text{Mg}_x\text{Zn}_{1-x}\text{O}$ the variation in the cohesive energy with the alloy composition x is almost linear. This is due to the fact that the variation between the different crystal structures as well as the variation in the excess energies with x for fixed crystal structure (cf. Fig. 2) both are small compared to the large difference of E_{coh} between ZnO and MgO. For that reason also, the temperature variation in the GQCA results is

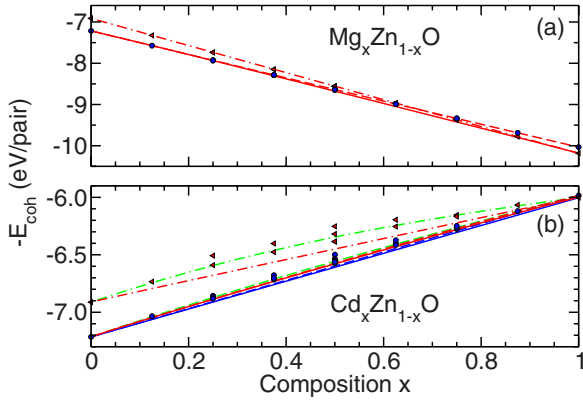


FIG. 9. (Color online) Negative cohesive energy E_{coh} (in electron volt per pair) of (a) $\text{Mg}_x\text{Zn}_{1-x}\text{O}$ and (b) $\text{Cd}_x\text{Zn}_{1-x}\text{O}$ alloys versus composition x . The curves are obtained using only wurtzite clusters (dashed line), only rocksalt clusters (dashed-dotted line), or both type of clusters (solid line). We use cluster fractions from the GQCA for $T=300$ K (blue curves) and $T=1100$ K (red curves), as well as ideal cluster fractions (green curves). The MDM result coincides with the one for from GQCA at room temperature. The cohesive energies are also shown for the clusters in rocksalt (red triangles) and wurtzite (blue circles) crystal structure.

not visible. Overall, neither for the rs nor the wz crystal structure, there is a visible dependence on the actual statistics that has been used.

For $\text{Cd}_x\text{Zn}_{1-x}\text{O}$ we find from Fig. 9(b) that the results within the GQCA and the SRS model differ. The curves from the MDM cannot be distinguished from the low-temperature GQCA results. For the wz crystal structure deviations resulting from the different statistics are small but visible. As discussed before, the mixed statistics gives rise to results that are close to those obtained when taking only wz clusters into account.

V. STRUCTURAL AND ELASTIC PROPERTIES

A. Fourfold bonding coordination

In Sec. IV, we found that especially for the $\text{Cd}_x\text{Zn}_{1-x}\text{O}$ system a significant fraction of the alloy locally shows the wz crystal structure over a large composition range. For that reason we investigate the behavior of the c lattice constant and the u parameter as characteristic parameters of the wz structure.

Figure 10(a) shows that in the case of $\text{Mg}_x\text{Zn}_{1-x}\text{O}$, the results from the GQCA for both temperatures and the curve obtained using the ideal cluster fractions almost coincide. The two statistics give rise to slightly larger values for c than the MDM and, therefore, also Vegard's law, which we find to be violated. Around $x=0.5$, the deviation may reach values of about 0.5%. As can be seen in Fig. 10(a), this leads to large errors when the composition of an alloy is determined by measuring the c -lattice constant and applying Vegard's rule.

Contrary, for $\text{Cd}_x\text{Zn}_{1-x}\text{O}$ [cf. Fig. 10(b)] the curves computed with the GQCA cluster fractions for high and low temperatures represent the two limiting cases. While the low-

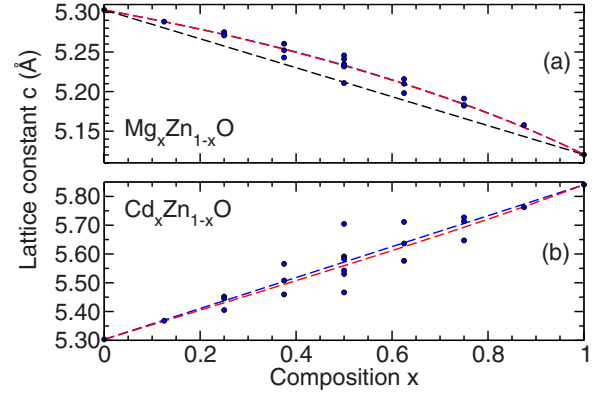


FIG. 10. (Color online) Lattice parameter c (in Å) of the wurtzite structure for (a) $\text{Mg}_x\text{Zn}_{1-x}\text{O}$ and (b) $\text{Cd}_x\text{Zn}_{1-x}\text{O}$ alloys with clusters in wz crystal structure only versus composition x . The black curves represent the MDM and the green curves the ideal cluster fractions. The GQCA results are shown for $T=300$ K (blue curve) and $T=1100$ K (red curve). For $\text{Mg}_x\text{Zn}_{1-x}\text{O}$, the GQCA curves and the SRS results coincide. For $\text{Cd}_x\text{Zn}_{1-x}\text{O}$, the low-temperature GQCA coincides with the MDM and the high-temperature GQCA with the result using ideal cluster fractions. Blue dots give the results for the individual clusters.

temperature curve coincides with the MDM, the high-temperature curve is close to the results from the SRS model and the deviations between the two cases are small.

A comparison of the values c_j for the individual clusters of both material systems shows that the variation is much larger for $\text{Cd}_{n_j}\text{Zn}_{n-n_j}\text{O}_{n_j}$ than for $\text{Mg}_{n_j}\text{Zn}_{n-n_j}\text{O}_{n_j}$. Overall, the deviations from the MDM (which is equivalent to Vegard's law) are larger for $\text{Mg}_x\text{Zn}_{1-x}\text{O}$ and we find a remarkable bowing of the curves which renders a purely linear interpolation questionable. Contrary, the bowing is smaller for $\text{Cd}_x\text{Zn}_{1-x}\text{O}$ despite the stronger deviations for individual clusters, e.g., with $n_j=3, 4$, or 5 Cd atoms.

In Fig. 11, we also study the influence of the cluster statistics on the internal cell parameter u of the hexagonal lattice, which describes the translation of the cation sublattice with respect to the anion sublattice along the c direction. Again, for $\text{Mg}_x\text{Zn}_{1-x}\text{O}$ there is a noticeable deviation of all statistics (that are almost equal) from the MDM result, with a remarkable bowing of the curves. The u values of the individual clusters show a larger scattering for $\text{Cd}_{n_j}\text{Zn}_{n-n_j}\text{O}_{n_j}$ than for $\text{Mg}_{n_j}\text{Zn}_{n-n_j}\text{O}_{n_j}$. In the case of $\text{Cd}_x\text{Zn}_{1-x}\text{O}$ again the low-temperature GQCA curve coincides with the MDM result while the high-temperature GQCA curve is close to the one obtained using ideal cluster fractions.

B. Cation-cation distance

Both crystal structures that are taken into account to describe the pseudobinary alloy system, rs and wz, are characterized by different lattice parameters. While the cubic rs structure is described by only one lattice constant a_0 , there are three independent parameters a , c , and u for the hexagonal wz structure which renders a universal description of the lattice structure of the alloys more difficult. As mentioned before, we solve this problem by restricting our discussion to

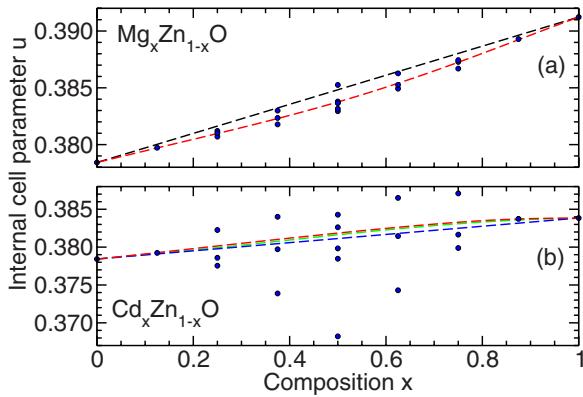


FIG. 11. (Color online) Internal cell parameter u of the wurtzite structure for (a) $\text{Mg}_x\text{Zn}_{1-x}\text{O}$ and (b) $\text{Cd}_x\text{Zn}_{1-x}\text{O}$ alloys derived from clusters in wz crystal structure only versus composition x . The black curves represent the MDM and the green curves the SRS model. The GQCA results are shown for $T=300$ K (blue curve) and $T=1100$ K (red curve). For $\text{Mg}_x\text{Zn}_{1-x}\text{O}$, the GQCA curves and the ideal cluster fractions coincide. For $\text{Cd}_x\text{Zn}_{1-x}\text{O}$, the low-temperature GQCA coincides with the MDM. Blue dots give the results for the individual clusters involved.

the average cation-cation distance $d_2(x)$. This quantity can be defined in a unique manner even for different crystal structures and is experimentally accessible at the same time. For the rs lattice, d_2 is simply related to the lattice constant a_0 by $d_2 = a_0/\sqrt{2}$ and for the ideal wz lattice with $c/a = \sqrt{8/3}$, it holds $d_2 = a$. We average over all cation-cation distances in one cluster to obtain the $d_{2,j}$ (cf. Tables II and III). Using the respective weights from the GQCA, the SRS model, and the MDM, the configurational average is calculated from Eq. (3) and the results are plotted in Fig. 12 for $\text{Mg}_x\text{Zn}_{1-x}\text{O}$ and $\text{Cd}_x\text{Zn}_{1-x}\text{O}$.

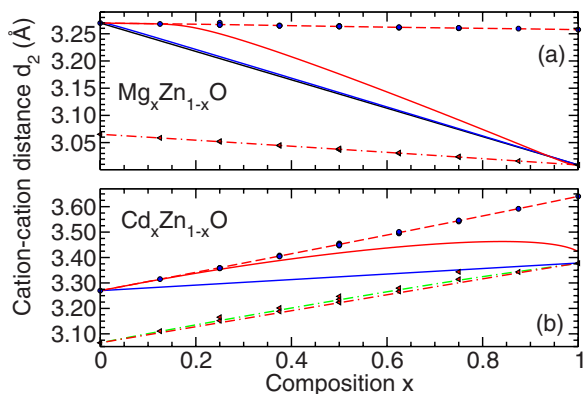


FIG. 12. (Color online) Average cation-cation (second-nearest neighbor) distance d_2 of (a) $\text{Mg}_x\text{Zn}_{1-x}\text{O}$ and (b) $\text{Cd}_x\text{Zn}_{1-x}\text{O}$ alloys versus composition x . The curves are obtained using the GQCA with wurtzite clusters only (dashed curves), rocksalt clusters only (dashed-dotted curves), or both types of clusters (solid curves). For the GQCA, we present results for $T=300$ K (blue curves) and $T=1100$ K (red curves). For comparison, we show results obtained using the MDM (black curves) and the SRS model (green curves). The cation-cation distances are also depicted for the individual clusters in rocksalt (red triangles) and wurtzite (blue circles) crystal structure.

For $\text{Mg}_x\text{Zn}_{1-x}\text{O}$ [cf. Fig. 12(a)], we find for the pure wz and pure rs cluster geometries that the three alloy statistics give almost the same results and, therefore, also agree well with Vegard's rule. For each fixed crystal structure, the variation in d_2 versus x is small whereas d_2 differs up to 8% between the wz and the rs structure of a material. While the GQCA results from the mixed statistics agrees well with the MDM for $T=300$ K, we find significant deviations for $T=1100$ K. In the high-temperature case, the cation-cation distance in the pseudobinary alloy remains very close to the value of the pure wz structure up to compositions of about $x \approx 0.2$ [cf. Fig. 12(a)]. For higher Mg contents, d_2 approaches the value of rs-MgO.

For $\text{Cd}_x\text{Zn}_{1-x}\text{O}$ [cf. Fig. 12(b)], the variation in d_2 is much larger than for $\text{Mg}_x\text{Zn}_{1-x}\text{O}$ since the cation-cation distance varies much more between ZnO and CdO. The results from all three statistics for the pure wz clusters and the pure rs clusters agree well with Vegard's rule except of a small deviation for the SRS model for rs-CdO. Again the most remarkable change is observed for the mixed cluster expansion. At room temperature, the curve connects the wz and rs end components almost linearly. For the higher temperature of $T=1100$ K, the cation-cation distance closely follows the wz trend up to Cd concentrations of more than 0.5. Overall, the different structural configurations can be clearly distinguished at fixed x via the average cation-cation distance. When both lattice structures can occur in the alloy we even find a more pronounced temperature dependence.

C. Bulk modulus

Besides the cation-cation distance we also study the bulk modulus B_0 for $\text{Mg}_x\text{Zn}_{1-x}\text{O}$ and $\text{Cd}_x\text{Zn}_{1-x}\text{O}$ using the three statistics evolving from the cluster weights of the GQCA, the SRS model, and the MDM. The results are plotted together with the values for the individual clusters in Fig. 13.

For $\text{Mg}_x\text{Zn}_{1-x}\text{O}$ [cf. Fig. 13(a)] in the pure rs or wz structure, the GQCA results show a temperature dependence and also differ from the linear interpolation of the MDM whereas the SRS curve is very close to the high-temperature result of the GQCA. The reason for this behavior is the stronger deviation of the bulk moduli for the individual clusters from the linear interpolation. As can be seen in Fig. 13(a) for the rs structure, we find a certain cluster with an especially low bulk modulus at $x=0.625$ which, therefore, coincides with the minimum of the GQCA curves. For the GQCA results using the mixed statistics, we find a strong temperature dependence since the room-temperature curve closely follows the MDM curve while the high-temperature result matches the pure wz curve up to $x \approx 0.2$ and then approaches the pure rs curve at $x=1$.

In the case of $\text{Cd}_x\text{Zn}_{1-x}\text{O}$ [see Fig. 13(b)], we find both GQCA curves for the pure rs lattice structure close to the MDM result. This is only true for the low-temperature result of the pure wz structure whereas the high-temperature curve differs remarkably in this case. For both rs and wz structure, the SRS model shows the largest deviation from the linear interpolation. Again this can be attributed to the stronger variation in the values for B_0 of the individual clusters with

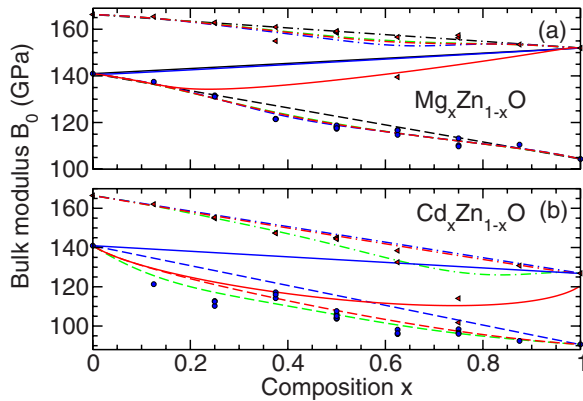


FIG. 13. (Color online) Bulk modulus B_0 (in GPa) of (a) $\text{Mg}_x\text{Zn}_{1-x}\text{O}$ and (b) $\text{Cd}_x\text{Zn}_{1-x}\text{O}$ alloys versus composition x . The curves are obtained using the GQCA with wurtzite clusters only (dashed curves), rocksalt clusters only (dashed-dotted curves), or both type of clusters (solid curves). For the GQCA, we present results for $T=300$ K (blue curves) and $T=1100$ K (red curves). For comparison, we also show results obtained using the MDM (black curves) and the SRS model (green curves). The bulk moduli are also depicted for the individual clusters in rocksalt (red triangles) and wurtzite (blue circles) crystal structure.

respect to the MDM curve with the strongest deviation occurring for rs at $x=0.75$ [cf. Fig. 13(b)]. For the mixed statistics for $\text{Cd}_x\text{Zn}_{1-x}\text{O}$, we find again that the low-temperature curve closely follows the linear interpolation while the high-temperature curve shows pronounced deviations. At low concentrations, it follows the high-temperature GQCA curve of the pure wz structure and does not even fully approach the rs limit due to the very small energetical difference of these two polymorphs for CdO (cf. Fig. 7).

VI. SUMMARY AND CONCLUSIONS

In summary, we studied pseudobinary $\text{A}_x\text{B}_{1-x}\text{C}$ alloys whose binary end components crystallize in different crystal structures under ambient conditions. To study $\text{Mg}_x\text{Zn}_{1-x}\text{O}$ and $\text{Cd}_x\text{Zn}_{1-x}\text{O}$ with rs (MgO, CdO) and wz (ZnO) equilibrium lattice structures, we adopted a cluster expansion for wz and presented a corresponding expansion for 16-atom rs clusters. To include simultaneously locally different bonding configurations with either fourfold (wz) or sixfold (rs) coordination, the GQCA has been extended correspondingly. Besides the GQCA which minimizes the mixing free energy with respect to the cluster fractions x_j , we took two other distributions x_j into account to simulate also certain nonequilibrium growth procedures. We have combined these methods with *ab initio* density-functional calculations using the

semilocal GGA to treat exchange and correlation. This provides knowledge of structural and energetic properties for each of the clusters which we use together with the cluster fractions to perform the configurational averages and, hence, to derive an averaged alloy property for given composition and temperature.

Correspondingly, we find that the alloys' thermodynamics is determined by the local chemical bonding and the cluster statistics and, therefore, the conditions under which the alloy is prepared. The mixing free energies indicate a change from preferred wz crystal structure to preferred rs crystal structure at about $x \approx 0.675$ for $\text{Mg}_x\text{Zn}_{1-x}\text{O}$ and about $x \approx 0.95$ for $\text{Cd}_x\text{Zn}_{1-x}\text{O}$. We find that for $\text{Mg}_x\text{Zn}_{1-x}\text{O}$ as well as $\text{Cd}_x\text{Zn}_{1-x}\text{O}$, the random alloy is always the most favorable. Only for $\text{Cd}_x\text{Zn}_{1-x}\text{O}$ in the SRS limit, we observe the occurrence of a miscibility gap and binodal as well as spinodal decomposition ranges with the critical parameters $T_{\text{crit}} = 1030$ K and $x_{\text{crit}} = 0.34$ for pure wz structure, $T_{\text{crit}} = 1940$ K and $x_{\text{crit}} = 0.4$ for the mixed statistics, and a critical temperature above 2500 K for pure rs crystal structure. In any case, we calculated even the temperature- and composition-dependent amount of wz and rs clusters in the system. The resulting ambivalent picture which is strongly dependent on the actual conditions, is verified by a variety of experimental results. For both material systems, there are experiments that agree with our predictions but also other experiments with deviating findings, showing that also measured properties of alloy films have to be related to growth conditions, deposition method, possible subsequent temper steps, etc.

For structural properties such as cation-cation distances and bulk moduli, we also find a significant dependence on the statistics that has been employed for the alloy modeling. In addition, the pronounced temperature dependence of the structural parameters and also the boundary conditions due to the growth mechanism should lead to distinct experimental observations of the alloy composition.

ACKNOWLEDGMENTS

We thank Lara K. Teles and R. Goldhahn for valuable discussions. The research leading to these results has received funding from the European Community's Seventh Framework Programme (FP7/2007-2013) under Grant Agreement No. 211956 and by the Deutsche Forschungsgemeinschaft (Project No. Be 1346/20-1). We acknowledge grants of computer time from the Supercomputerzentrum Stuttgart and the HPC-EUROPA2 project (Project No. 228398) with the support of the European Commission—Capacities Area—Research Infrastructures. A.S. thanks the Carl-Zeiss-Stiftung for support.

¹D. C. Reynolds, D. C. Look, and B. Jogai, *Solid State Commun.* **99**, 873 (1996).

²D. C. Reynolds, D. C. Look, B. Jogai, and T. C. Collins, *Phys. Rev. B* **56**, 13753 (1997).

³M. Joseph, H. Tabata, and T. Kawai, *Jpn. J. Appl. Phys., Part 2*

38, L1205 (1999).

⁴Ü. Özgür, Y. I. Alivov, C. Liu, A. Teke, M. A. Reshchikov, S. Doğan, V. Avrutin, S.-J. Cho, and H. Morköç, *J. Appl. Phys.* **98**, 041301 (2005).

⁵D. S. Ginley and C. Bright, *MRS Bull.* **25**, 15 (2000).

- ⁶S. Tsukazaki, A. Ohtomo, T. Kita, Y. Ohno, H. Ohno, and M. Kawasaki, *Science* **315**, 1388 (2007).
- ⁷A. P. Ramirez, *Science* **315**, 1377 (2007).
- ⁸L. Schmidt-Mende and J. L. MacManus-Driscoll, *Mater. Today* **10**, 40 (2007).
- ⁹A. Ohtomo and A. Tsukazaki, *Semicond. Sci. Technol.* **20**, S1 (2005).
- ¹⁰R. Schmidt, B. Rheinländer, M. Schubert, D. Spemann, T. Butz, J. Lenzner, E. M. Kaidashev, M. Lorenz, A. Rahm, H. C. Semmelhack, and M. Grundmann, *Appl. Phys. Lett.* **82**, 2260 (2003).
- ¹¹S. Sadofev, S. Blumstengel, J. Cui, J. Puls, S. Rogaschewski, P. Schäfer, Y. G. Sadofyev, and F. Henneberger, *Appl. Phys. Lett.* **87**, 091903 (2005).
- ¹²S. Sadofev, S. Blumstengel, J. Cui, J. Puls, S. Rogaschewski, P. Schäfer, and F. Henneberger, *Appl. Phys. Lett.* **89**, 201907 (2006).
- ¹³S. Shigemori, A. Nakamura, J. Ishihara, T. Aoli, and J. Temmyo, *Jpn. J. Appl. Phys.* **43**, L1088 (2004).
- ¹⁴*Springer Handbook of Condensed Matter and Materials Data*, edited by W. Martienssen and H. Warlimont (Springer-Verlag, Berlin, 2005).
- ¹⁵A. Schleife, F. Fuchs, J. Furthmüller, and F. Bechstedt, *Phys. Rev. B* **73**, 245212 (2006).
- ¹⁶M. Sanati, G. L. W. Hart, and A. Zunger, *Phys. Rev. B* **68**, 155210 (2003).
- ¹⁷E. Segnit and A. Holland, *J. Am. Ceram. Soc.* **48**, 409 (1965).
- ¹⁸C. Bundesmann, A. Rahm, M. Lorenz, M. Grundmann, and M. Schubert, *J. Appl. Phys.* **99**, 113504 (2006).
- ¹⁹Z. Liu, Z. Mei, T. Zhang, Y. Liu, Y. Guo, X. Du, A. Hallen, J. Zhu, and A. Kuznetsov, *J. Cryst. Growth* **311**, 4356 (2009).
- ²⁰X. Du, Z. Mei, Z. Liu, Y. Guo, T. Zhang, Y. Hou, Z. Zhang, Q. Xue, and A. Y. Kuznetsov, *Adv. Mater.* **21**, 4625 (2009).
- ²¹J. Chen, W. Z. Shen, N. B. Chen, D. J. Qiu, and H. Z. Wu, *J. Phys.: Condens. Matter* **15**, L475 (2003).
- ²²N. B. Chen, H. Z. Wu, D. J. Qiu, T. N. Xu, J. Chen, and W. Z. Shen, *J. Phys.: Condens. Matter* **16**, 2973 (2004).
- ²³T. Makino, Y. Segawa, M. Kawasaki, A. Ohtomo, R. Shiroki, K. Tamura, T. Yasuda, and H. Koinuma, *Appl. Phys. Lett.* **78**, 1237 (2001).
- ²⁴F. Bertram, S. Giemsch, D. Forster, J. Christen, R. Kling, C. Kirchner, and A. Waag, *Appl. Phys. Lett.* **88**, 061915 (2006).
- ²⁵W. R. Lambrecht, S. Limpitjumnong, and B. Segall, *MRS Internet J. Nitride Semicond. Res.* **4S1**, G6.8 (1999).
- ²⁶R. Thangavel, M. Rajagopalan, and J. Kumar, *Solid State Commun.* **137**, 507 (2006).
- ²⁷E. C. Lee, Y. S. Kim, Y. G. Jin, and K. J. Chang, *J. Korean Phys. Soc.* **39**, S23 (2001).
- ²⁸S.-H. Wei, L. G. Ferreira, J. E. Bernard, and A. Zunger, *Phys. Rev. B* **42**, 9622 (1990).
- ²⁹A.-B. Chen and A. Sher, *Semiconductor Alloys* (Plenum, New York, 1995).
- ³⁰L. K. Teles, J. Furthmüller, L. M. R. Scolfaro, J. R. Leite, and F. Bechstedt, *Phys. Rev. B* **62**, 2475 (2000).
- ³¹J. M. Sanchez, F. Ducastelle, and D. Gratias, *Physica A* **128**, 334 (1984).
- ³²A. Zunger, in *Statistics and Dynamics of Alloy Phase Transformations*, edited by P. E. A. Turchi and A. Gonis (Plenum Press, New York, 1994), p. 361.
- ³³J. Z. Liu and A. Zunger, *Phys. Rev. B* **77**, 205201 (2008).
- ³⁴A. Sher, M. van Schilfgaarde, A.-B. Chen, and W. Chen, *Phys. Rev. B* **36**, 4279 (1987).
- ³⁵C. Caetano, L. K. Teles, M. Marques, A. Dal Pino, Jr., and L. G. Ferreira, *Phys. Rev.* **74**, 045215 (2006).
- ³⁶X. F. Fan, H. D. Sun, Z. X. Shen, J.-L. Kuo, and Y. M. Lu, *J. Phys.: Condens. Matter* **20**, 235221 (2008).
- ³⁷I. V. Maznichenko, A. Ernst, M. Bouhassoune, J. Henk, M. Däne, M. Lüders, P. Bruno, W. Hergert, I. Mertig, Z. Szotek, and W. M. Temmerman, *Phys. Rev. B* **80**, 144101 (2009).
- ³⁸J. W. D. Connolly and A. R. Williams, *Phys. Rev. B* **27**, 5169 (1983).
- ³⁹A. Zunger, S.-H. Wei, L. G. Ferreira, and J. E. Bernard, *Phys. Rev. Lett.* **65**, 353 (1990).
- ⁴⁰S.-H. Jeong, B.-S. Kim, and B.-T. Lee, *Appl. Phys. Lett.* **82**, 2625 (2003).
- ⁴¹L. Vegard, *Z. Phys.* **5**, 17 (1921).
- ⁴²P. Hohenberg and W. Kohn, *Phys. Rev.* **136**, B864 (1964).
- ⁴³W. Kohn and L. J. Sham, *Phys. Rev.* **140**, A1133 (1965).
- ⁴⁴G. Kresse and J. Furthmüller, *Phys. Rev. B* **54**, 11169 (1996).
- ⁴⁵J. P. Perdew, in *Electronic Structure of Solids '91*, edited by P. Ziesche and H. Eschrig (Akademie-Verlag, Berlin, 1991), p. 11.
- ⁴⁶J. P. Perdew and Y. Wang, *Phys. Rev. B* **45**, 13244 (1992).
- ⁴⁷A. Schleife, F. Fuchs, C. Rödl, J. Furthmüller, and F. Bechstedt, *Phys. Status Solidi B* **246**, 2150 (2009).
- ⁴⁸A. Schleife, C. Rödl, F. Fuchs, J. Furthmüller, and F. Bechstedt, *Phys. Rev. B* **80**, 035112 (2009).
- ⁴⁹A. Janotti, D. Segev, and C. G. Van de Walle, *Phys. Rev. B* **74**, 045202 (2006).
- ⁵⁰F. Oba, A. Togo, I. Tanaka, J. Paier, and G. Kresse, *Phys. Rev. B* **77**, 245202 (2008).
- ⁵¹P. E. Blöchl, *Phys. Rev. B* **50**, 17953 (1994).
- ⁵²G. Kresse and D. Joubert, *Phys. Rev. B* **59**, 1758 (1999).
- ⁵³H. J. Monkhorst and J. D. Pack, *Phys. Rev. B* **13**, 5188 (1976).
- ⁵⁴F. D. Murnaghan, *Proc. Natl. Acad. Sci. U.S.A.* **30**, 244 (1944).
- ⁵⁵*Table of Periodic Properties of Elements* (Sargent-Welch, Skokie, Illinois, 1980).
- ⁵⁶L. Zhang and H. Huang, *Appl. Phys. Lett.* **90**, 023115 (2007).
- ⁵⁷J. Carrasco, F. Illas, and S. T. Bromley, *Phys. Rev. Lett.* **99**, 235502 (2007).
- ⁵⁸A. Seko, F. Oba, A. Kuwabara, and I. Tanaka, *Phys. Rev. B* **72**, 024107 (2005).
- ⁵⁹S. Limpitjumnong and S. Jungthawan, *Phys. Rev. B* **70**, 054104 (2004).
- ⁶⁰J. Ishihara, A. Nakamura, S. Shigemori, T. Aoki, and J. Temmyo, *Appl. Phys. Lett.* **89**, 091914 (2006).
- ⁶¹T. Minemoto, T. Negami, S. Nishiwaki, H. Takakura, and Y. Hamakawa, *Thin Solid Films* **372**, 173 (2000).
- ⁶²Z. Vashaei, T. Minegishi, H. Suzuki, T. Hanada, M. W. Cho, T. Yao, and A. Setiawan, *J. Appl. Phys.* **98**, 054911 (2005).
- ⁶³A. Ohtomo, M. Kawasaki, T. Koida, K. Masubuchi, H. Koinuma, Y. Sakurai, Y. Yoshida, T. Yasuda, and Y. Segawa, *Appl. Phys. Lett.* **72**, 2466 (1998).